Received: 3 November 2022 | Revised: 26 December 2022 | Accepted: 11 January 2023

DOI: 10.1002/aoc.7021

RESEARCH ARTICLE

Applied Organometallic Chemistry WILEY

Pyridine derivatives complexes of Co(II) and Ni(II) 3-bromobenzoates: Crystal structure, in silico anti-SARS-CoV-2 potential, serum albumin binding properties and cytotoxicity

Füreya Elif Öztürkkan[1] | **Mücahit Özdemir**[2] | **Giray Buğra Akbaba**[3] | **Mustafa Sertçelik**[1] | **Bahattin Yalçın**[2] | **Ertan Şahin**[4]

[1]Department of Chemical Engineering, Kafkas University, Kars, Turkey

[2]Department of Chemistry, Marmara University, Istanbul, Turkey

[3]Department of Bioengineering, Kafkas University, Kars, Turkey

[4]Department of Chemistry, Atatürk University, Erzurum, Turkey

Correspondence
Füreya Elif Öztürkkan, Department of Chemical Engineering, Kafkas University, Kars, Turkey.
Email: fozturkkan36@gmail.com

Funding information
Kafkas University Research Fund, Grant/Award Number: 2018-FM-66

Two mononuclear $[Co(3\text{-}BrBA)_2(NA)_2(H_2O)_2]$ (**1**) and $[Ni(3\text{-}BrBA)_2(3\text{-}CNPY)_2(H_2O)_2]$ (**2**) (3-BrBA = 3-bromobenzoate, NA = pyridine-3-carboxylic acid, and 3-CNPy = 3-cyanopyridine) were synthesized and characterized by single crystal X-ray diffraction, elemental analysis, and FT-IR spectroscopy. In both complexes, the metal atom is coordinated by two oxygen atoms of two carboxylate anions, two nitrogen atoms of two pyridine rings, and two oxygen atoms of two water molecules in the distorted octahedral environment. Intermolecular interactions were examined with the help of the 3D Hirshfeld surfaces and 2D fingerprint plots. With the help of density functional theory (DFT) studies, besides verifying the experimentally obtained structural properties, the electronic energies, polarizability, dipole moments, ionization potentials, electron affinities, electronegativity, chemical hardness, global softness, electrophilic indexes, HOMO-LUMO orbitals, and band gaps were also calculated. In vitro cytotoxic activity of the complexes on primary peripheral blood mononuclear cells were evaluated using the MTT assay. Fluorescence quenching techniques and molecular docking studies were used to investigate the interaction between bovine serum albumin (BSA) and the complexes. The molecular docking study has been used to explain the interaction of complexes with spike proteins of beta variant (B.1.351), gamma variant (P.1), delta variant (B.1.617.2), kappa variant (B.1.617.1), and omicron variant (B.1.1.529) of coronavirus. Additionally, the pharmacokinetic and toxicological properties of the complexes have been computed using the SwissADME and ProTox-II online databases, respectively.

KEYWORDS
ADMET, arylcarboxylate, BSA, molecular docking, SARS CoV-2

1 | INTRODUCTION

Coordination compounds containing metal–organic ligands framework are known as interesting materials due to their interesting structural properties, potential applications in many areas,[1–3] and their biological importance.[4] The structures of these complexes vary depending on the metal atom–ligand relationship and reaction conditions.[5] Moreover, the biological properties of these complexes are generally related to the coordination ability of the metal ion.[6,7] There are many studies on the biological properties such as antibacterial,[8] antifungal,[8] antioxidant,[9] anticholinesterase,[10] anticancer,[6,7] antiviral,[8,9] and DNA binding activity[11] of the metal-arylcarboxylate complexes containing N–, O–donor ligands. Many previous studies have emphasized that these complexes have drug potential.

Severe acute respiratory syndrome-coronavirus-2 (SARS-CoV-2) disease, 2019 (COVID-19), has caused a global pandemic that continues to threaten many lives around the world.[12] SARS-CoV-2 has a wide clinical spectrum leading to asymptomatic infection, respiratory failure, and even death.[13] So far, some of the described variants of SARS CoV-2, B.1.1.7 (Alpha variant), B.1.351 (Beta variant), B.1.1.28 (Gamma variant), B.1.525 (eta variant), B.1.617.1 (kappa variant), B.1.427/B.1.429 (epsilon variant), B.1.617.2 (Delta variant), and B.1.1.529 (Omicron variant).[14,15] According to the findings of many studies, the variants are responsible for the increased infectivity, effectiveness, and severity of the disease. Numerous studies showed that these variants increase the affinity of the spike receptor-binding domain (RBD) to bind to the angiotensin-converting enzyme 2 (ACE2) receptor.[16] Studies related to the identification of variants and the identification of the effects of the disease have improved the acceleration of treatment-oriented studies, and the uncertainties at the beginning of the pandemic have been reduced thanks to these data. When the effects on humanity are considered, treatment for this disease is a must. However, drug treatment, which is a common problem of many viral diseases, is also valid for this disease. The importance of theoretical research emerges when the duration of drug research development studies is taken into account.[17] Scientists are struggling to create anti-CoV2 drugs and vaccines specific to SARS-CoV-2 due to the high rate of mutation and recombination.[18] Therefore, it is important to know the effects of drug candidate compounds on various variants. Although some metal arylcarboxylate complexes exhibit antiviral properties against some viruses, studies on the drug potential of SARS CoV-2 were limited. In this context, we synthesized pyridine 3-carboxylate/3-cyanopyridine complexes of Co(II) and Ni(II) 3-bromobenzoate in this study. Elemental analysis, single crystal X-ray diffraction, mass spectrometry, and FT-IR spectroscopy methods were used for the structural characterization of the complexes. The cytotoxic effects of the complexes on human blood lymphocyte cells were determined by the MTT assay. The interactions of SARS CoV-2 variants with the active site of the spike protein were determined by molecular docking studies. In addition, its pharmacokinetic and toxicological properties (ADMET calculations) were determined with the help of online databases.

2 | MATERIALS AND METHODS

2.1 | Chemicals and instruments

3-Bromobenzoic acid (Fluka), nicotinamide (Fluka), 3-cyanopyridine (Sigma Aldrich), sodium bicarbonate (Merck), nickel (II) sulfate hexahydrate (Merck), and cobalt (II) sulfate heptahydrate (Sigma Aldrich) were purchased commercially and used without pre-treatment. Phosphate Buffered saline solution, dimethyl sulfoxide (DMSO), Dulbecco's modified Eagle medium and fetal bovine serum (FBS) (Sigma-Aldrich, Germany), 3-(4,5-dimethylthiazol-2-yl)-2,5-diphenyltetrazolium bromide (MTT), and penicillin/streptomycin (Thermo Fisher Scientific) used for the evaluation of cytotoxic activity were purchased commercially.

The C, N, and N microelemental analyses were determined with the LECO CHNS-932 elemental analyzer. FT-IR spectra were taken in the range of 4000–600 cm^{-1} from solid samples with the Perkin Elmer Frontier™ FT-IR Spectrometer, which has an ATR detector. In cytotoxicity studies, Hed Lab X BIO MSC CLASS II Biosafety cabinet, Thermo Fisher EVOS FL Inverted Microscope, Panasonic MCO-170AICUVH-PE CO_2 Incubator, and BioTek Epoch UV-Vis Spectrophotometer were used.

2.2 | Synthesis of diaquabis(pyridine 3-carboxylate-κN^1)-bis(3-bromobenzoate-κO)cobalt (II) (1)

Sodium bicarbonate (840 mg, 10 mmol) and 3-bromobenzoic acid were mixed in 50 ml of water at about 60°C until all of the carbon dioxide gas was removed. As a result of this reaction, sodium 3-bromobenzoate was obtained. A solution of nicotinamide (1220 mg, 10 mmol) in 20 ml of distilled water and a previously obtained of sodium 3-bromobenzoate solution (2010 mg, 10 mmol) was added to the $CoSO_4{\cdot}7H_2O$

(1400 mg, 5 mmol) in 20-ml distilled water solution, respectively. At room temperature, this mixture was allowed to stand, and pink crystals formed within 2 weeks. The crystals obtained were filtered, washed with distilled water, and dried in the open air at room temperature. Yield: 85.21% (6.32 g). Anal. Calc. for $\mathbf{C_{26}H_{24}N_4O_8CoBr_2}$: C, 42.92; H, 3.40; N, 7.53%. Found: C, 42.24; H, 3.27; N, 7.58%. IR (cm^{-1}): 3444w, 3359m, 3324m, 3050w, 1689s, 1640m, 1587s, 1383s, 1064m, 830s, 637s, 787s.

2.3 | Synthesis of diaquabis(3-cyanopyridine-κN^1)-bis (3-bromobenzoate-κ*O*)nickel (II) (2)

Complex **2** was prepared following the procedure in the synthesis of complex **1** above. A solution of 3-cyanopyridine (1040 mg, 10 mmol) in 20 ml of distilled water and a previously prepared solution of sodium 3-bromobenzoate (2010 mg, 10 mmol) was added to the $NiSO_4{\cdot}6H_2O$ (1310 mg, 5 mmol) in 20-ml distilled water solution, respectively. The mixture was left to stand at room temperature, and green crystals formed within 3 weeks. The resulting crystals were filtered, washed with distilled water, and allowed to air dry at room temperature. Yield: 87.09% (6.12 g). Anal. Calc. for $\mathbf{C_{26}H_{20}N_4O_6NiBr_2}$: C, 44.55; H, 2.98; N, 7.95%. Found: C, 44.42; H, 2.87; N, 7.97%. IR (cm^{-1}): 3481w, 3080w, 2236w, 1597s, 1575m, 1407s, 1032m, 826s, 646s, 767s.

2.4 | Crystal structure determination

Single crystals of the Co^{II} (**1**) and Ni^{II} (**2**) complexes were employed for the data collection on a four-circle Rigaku R-AXIS RAPID-S diffractometer (equipped with a two-dimensional area IP detector) in order to identify the crystal structure. Graphite-monochromated Mo-K_α radiation ($\lambda = 0.71073$ Å) and oscillation scans technique with $\Delta w = 5°$ for one image were used for data collection. On the basis of all reflections with F2 > 2, the lattice parameters were calculated using least-squares techniques (F2). Integration of the intensities, correction for Lorentz and polarization effects, and cell refinement was performed using CrystalClear (Rigaku/MSC Inc., 2005) software.[19] SHELXS-2013 was used to solve the structures utilizing direct methods,[20] which allowed the location of most of the heaviest atoms, with the remaining nonhydrogen atoms being located from difference Fourier maps calculated from successive full-matrix least-squares refinement cycles on F^2 using SHELXL-2013.[21] All nonhydrogen atoms were refined using anisotropic displacement parameters. The hydrogen atoms were given common isotropic displacement factors and were incorporated in the last refinement utilizing geometrical restraints. The final difference in Fourier maps revealed no chemically significant peaks.

2.5 | Cytotoxicity studies

Primary peripheral blood mononuclear cells (PCS-800-011) were grown at 37°C with 5% CO_2 in DMEM (high glucose) supplemented with 10% (v/v) fetal bovine serum and 1% penicillin/streptomycin. The following working concentrations were determined: 1000, 500, 250, 125, 62.5, 31.25, 15.63, and 7.81 ppm. All solutions were made with ultrapure water; 100 µl of culture media was supplied to the 96-well microplates. Each well received an addition of 100 µl (5000 cells). The microplates were incubated in an incubator at 37°C and 5% CO_2 for 24 h to allow the cells to attach to the surface. Then, 100-µl aliquots of different concentrations of the tested complexes were added to the wells containing the culture medium and incubated again for 24 h. Following the incubation period, each well received 10 µl of MTT reagent, which was added to PBS at a concentration of 5 mg/ml, and incubation was continued for another 4 h. After the incubation was completed, the medium was completely removed from the wells; 200 µl of DMSO was added to each well to dissolve the resulting formazan. After 18 h of incubation, the absorbance of the microplates was recorded using a spectrophotometer at 570 nm. By comparing the cell to the control group (200 µl of culture media), cell viability was evaluated.[22]

2.6 | Bovine serum albumin (BSA) titration

1×10^{-6} M BSA prepared in PBS was determined spectrofluorometrically using the quenching coefficient of BSA. BSA titration is performed by adding complexes **1** and **2** to the BSA solution (solution concentration = 1×10^{-6} M) in concentration ranges of 0–50 µM. The lifetime value of the BSA molecule is 10^{-8} s (10 ns).[23–25]

2.7 | Theoretical studies

Density functional theory (DFT)[26] was used to investigate molecular structures and molecular properties. The molecular structures of investigated molecules were optimized by Gaussian09[27] in the gas phase and visualized

by IQMol.[28] The B3LYP functional[29–31] was used for DFT with the 6-311G** basis set. True minimum natures of optimized structures were verified with all positive frequencies.

To visualize the intermolecular interactions in complexes **1** and **2**, a Hirshfeld surface analysis[32] was performed using CrystalExplorer21.[33]

Autodock Vina[34] was used to do a molecular docking study on target proteins for complexes **1** and **2** to estimate inhibition properties. Crystal structures of variants of spike proteins of SARS-CoV-2 were obtained from the protein data bank (https://www.rcsb.org/). The 3D molecular structures of the ligands were obtained from the crystal file (.cif). Water molecules were removed from the crystal files so that the steric hindrance does not affect the binding scores and does not keep bulky ligands away from the active site. The missing polar hydrogens and Kollman charges on the crystal data were added. Lamarckian genetic algorithm[35] was chosen as an insertion engine. Inhibitors with the lowest energy insertion score were selected from the 10 conformations as a result of the calculation. To increase the reliability of molecular docking calculations, 10 same calculations were made, and binding affinity values were calculated with standard deviation. Discovery Studio Visualizer v21.1.0.20298[36] was used to visualize the molecular docking results.

Identifying the pharmacokinetic and toxicokinetic properties of drug candidate molecules eliminates the need for extra studies in drug development, saving time and money while improving the success rate. The absorption, distribution, metabolism, excretion, and toxicity (ADMET) criteria must have defined the properties of a medicinal chemical. The SwissADME online database[37] was used to calculate the complex's absorption, distribution, metabolism, and excretion values. To determine toxicity levels, the ProTox-II online database[38] was used.

3 | RESULTS AND DISCUSSION

3.1 | Crystal structure description

Crystal and structure refinement data of the Co^{II} (**1**) and Ni^{II} (**2**) complexes were given in Table 1. The asymmetric unit of diaquabis(3-bromobenzoato)-bis(pyridine-3-carboxylic acid) cobalt; Co(3-bromobenzoate)$_2$(NA)$_2$(H$_2$O)$_2$ (1), consists of one crystallographically independent Co(II) cation, located on a center of inversion, as well as one 3-bromobenzoate (BNZ) anion, one nicotinic acid ligand, and one aqua molecule occupying general positions. The complex comprises two deprotonated bromobenzoate ligands in a monodentate coordination mode and two nicotinic acid ligands. A slightly distorted CoN_2O_4 coordination sphere is completed by two aqua ligands (Figure 1). The Co^{II} cation is octahedrally coordinated. The bond angles of the octahedron vary appreciably from the ideal ones and are in the range of 91.76–86.12° and indicate somewhat distortion from perfect octahedral geometry. The four oxygen atoms occupy the equatorial plane of the complex in a *trans* configuration, and the NA ligands are coordinated through their N atoms in the axial positions. The Co-N pyridine bond length is 2.177(4) Å. The Co-O bond length of the BNZ ligand is 2.032 (3) Å, which is shorter than the terminal water ligand of 2.141 (4) Å as expected. The bond lengths determined for this structure (Table 2) are consistent with the literature.[39,40]

Intramolecular O3-H···O1 [2.606(5) Å] hydrogen bonding is observed between the carboxylate oxygen atoms and the coordinating water molecules, generating an *S*(6) ring motif. The packing of complex **1** is controlled by a series of O-H···O, C-H···O hydrogen bridges, and O···Br halogen bonds (Table 3).

The numbering scheme of the Ni(II) complex is shown in Figure 2. Selected bond lengths and angles are listed in Table 2. The asymmetric unit of the diaquabis(3-bromobenzoato)-bis(pyridine-3-carbonitrile)-nickel (II); Ni(NN)$_2$(bromobenzoate)$_2$(H$_2$O)$_2$ (**2**), consists of one Ni^{II} cation, one 3-bromobenzoate anion, one water molecule, and one neutral nicotinonitrile (NN) co-ligand. The cation is in an inversion center, whereas all of the ligands are in general locations. The Ni^{II} cation is coordinated by two terminal O-bound inorganic 3-bromobenzoate anions, two water molecules, and two nicotinonitrile ligands that are coordinated via the pyridine ring's nitrogen atom in an all-*trans* configuration. In the Ni(II) complex, as in the cobalt complex (**1**), the coordination is octahedral. The bond angles of the octahedron are in the range of 93.37–85.24° and indicate distortion. The distortion here is more than complex **1**. Within the scope of our ongoing work, the crystal structures of similar Co^{II} and Ni^{II} complexes [Co(C$_6$H$_6$N$_2$O)$_2$(C$_7$H$_4$NO$_4$)$_2$(H$_2$O)$_2$],[41] [Co(C$_9$H$_9$O$_2$)$_2$(C$_{10}$H$_{14}$N$_2$O)$_2$(H$_2$O)$_2$],[42] [Ni(C$_7$H$_4$ClO$_2$)$_2$(C$_6$H$_6$N$_2$O)2(H$_2$O)$_2$],[43] have also been reported.

Similar to complex **1**, complex **2**'s hydrogen bonds are crucial for ensuring molecule stability. Here, the S(6) ring motif is formed, which is again caused by the intramolecular hydrogen bonding (O3-H ···O2) between the benzoate and aqua units. The intermolecular hydrogen bond interactions of complex **2** are displayed in Figure 2b. Here, the O···Br halogen bond is shorter than the sum of van der Waals distances and in the same order as the interaction in the cobalt (II) (**1**) complex (Table 3).

TABLE 1 Crystal and structure refinement data of the Co^{II} (**1**) and Ni^{II} (**2**) complexes

	1	**2**
Empirical formula	$C_{26}H_{22}N_2O_{10}Br_2Co$	$C_{26}H_{20}N_4O_6Br_2Ni$
Formula weight	741.2	702.99
Temperature (K)	293(2)	293(2)
Wavelength (Å)	0.71073	0.71073
Crystal system	monoclinic	monoclinic
Space group	$P2_1/n$	$P2_1/n$
Unit cell dimensions (Å,°)	$a = 11.6193(9)$	$a = 11.5152(6)$
	$\alpha = 90$	$\alpha = 90$
	$b = 8.7871(8)$	$b = 8.5253(5)$
	$\beta = 90.053(5)$	$\beta = 91.52(2)$
	$c = 13.8205(9)$	$c = 14.0894(4)$
	$\gamma = 90$	$\gamma = 90$
Volume ($Å^3$)	1411.07(9)	1382.68(9)
Z	2	2
Density (calculated) (g/cm^3)	1.744	1.689
Absorption coefficient (mm^{-1})	3.499	3.639
$F(000)$	738	700
Theta range for data collection (°)	2.9 to 25.4	2.9 to 26.6
Index ranges	$-13 \le h \le 13, -14 \le k \le 14, -14 \le l \le 14$	$-14 \le h \le 14, -10 \le k \le 10, -17 \le l \le 17$
Reflections collected	34,878	16,936
Independent reflections	2610 [R(int) = 0.053]	2831 [R(int) = 0.10]
Data Completeness (%)	99.5	98.0
Refinement method	Full-matrix least-squares on F^2	Full-matrix least-squares on F^2
Data/restraints/parameters	2432/0/189	1509/0/179
Goodness-of-fit on F^2	1.224	1.646
Final R indices [$I > 2$sigma(I)]	$R1 = 0.083$, w$R2 = 0.098$	$R1 = 0.085$, w$R2 = 0.146$
R indices (all data)	$R1 = 0.120$, w$R2 = 0.218$	$R1 = 0.134$, w$R2 = 0.176$
Largest diff. peak and hole	1.90 and 1.878	1.718 and 0.996
CCDC number	2152498	2155631

Note: CCDC-2152498 (**1**) and 2155631 (**2**) numbers contain supplementary crystallographic data for this structure (12). These data are provided free of charge via the joint CCDC/FIZ Karlsruhe deposition service www.ccdc.cam.ac.uk/structures.

3.2 | FT-IR results

The absorption bands of functional groups in the complexes' structures were determined by FT-IR spectroscopy. Asymmetric and symmetrical N–H bands were reported at 3300–3100 cm^{-1}.[44–46] Asymmetric and symmetrical N–H vibrations of complex **1** were observed at 3359 and 3324 cm^{-1}, respectively. Aromatic C–H vibrations of complexes **1** and **2** were observed as moderately strong bands in the range of 3150–2900 cm^{-1}. Previous research has found that the nicotinamide ligand's carboxamide group C=O stretching vibration occurs at 1660 cm^{-1}. The $\Delta\upsilon$ value, which is determined by comparing the asymmetric and symmetric COO-group vibrations, provides details regarding the kind of coordination of the carboxylate group. The fact that this value is close to 200 cm^{-1} confirms the monodentate coordination type. The $\Delta\upsilon$ for complexes **1** and **2** were found to be 204 cm^{-1} and 190 cm^{-1}, respectively.[47] The crystal structure determined by single crystal X-ray diffraction also confirms the monodentate coordination type. C–N absorption bands in the pyridine ring of the 3-cyanopyridine ligand were seen at 2236 cm^{-1}. The absorption bands of 1,3-disubstituted benzene for

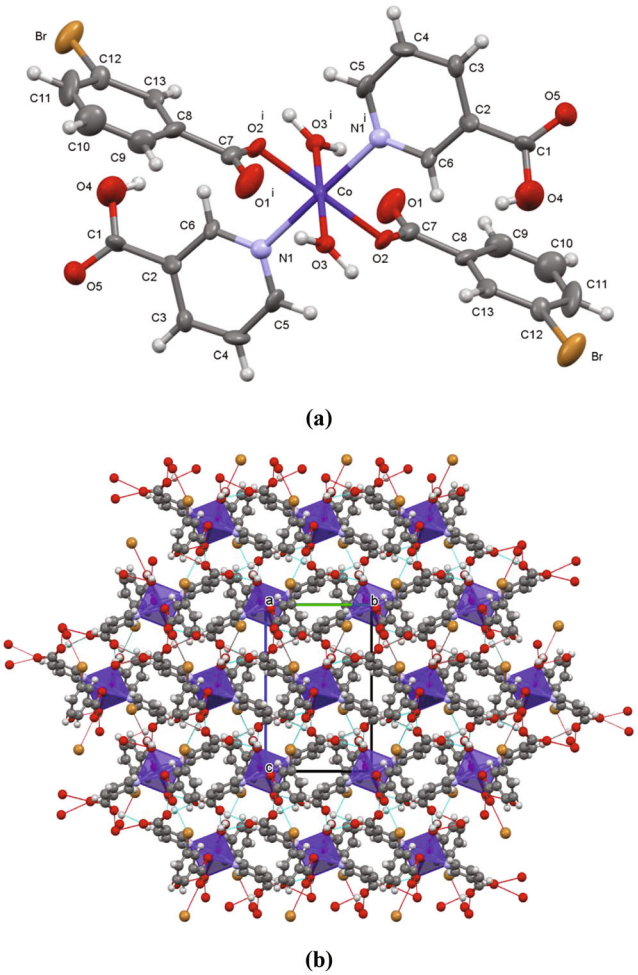

FIGURE 1 (a) Molecular structure of the Co(II) complex **1**. Displacement ellipsoids were drawn at the 40% probability level. (b) 2D-coordination polyhedra around the Co^{II} atoms with the unit cell viewed down along the *a*-axis. Dashed red lines indicate 2D halogen and *H*-bonding networks in complex **1**. Symmetry (i) 1 − x,1 − y,1 − z

complexes **1** and **2** were found at 830 cm^{-1} and 826 cm^{-1}, respectively. When the experimental and theoretical data of the absorption bands of the functional groups of complexes **1** and **2** in Table S1 are evaluated, the results are found to be in good agreement.

3.3 | Hirshfeld surface analysis

Hirshfeld surfaces allow for the display of diverse colors and intensities of intermolecular interactions, showing short or long contacts as well as the intensity of interactions.[48] Figures 4a and 5a show the dnorm maps of complexes **1** and **2**. On the dnorm maps,[49] the red spots show close contacts attributable to the O-H···O hydrogen bonds.[50] Donor and acceptor groups are represented on the shape-index for complexes **1** and **2** respectively by convex blue areas and concave red areas (Figures S1a and S2a). The crystal structures of complexes **1** and **2** exhibit π-π stacking interactions, as can be observed by looking at the neighboring red and blue triangles (Figures S1b and S2b). Significant intermolecular interactions of complexes **1** and **2** were mapped in Figures S3 and S4. On the Hirshfeld surfaces of the complexes **1** and **2**, the H···H interactions were observed in the large region (23.9% for 1 and 20.6% for 2) of the fingerprint plot at $d_i = d_e = 1.11$ Å and $d_i = d_e = 0.98$ Å, respectively. In the presence of O–H···O hydrogen bond interactions, the pair of characteristic spikes attributed to H···O/O···H interactions were observed in the fingerprint plot have the tips at $d_i + d_e = 2.08$ Å for complex **1** and 2.42 Å for complex **2**. The fingerprint plot's H···C/C···H interactions-delineated pair of wings has a symmetrical distribution of points and have the tips at $d_i + d_e = 2.88$ Å for both complexes. The percentage contribution of H···Br/Br···H interactions to the packing for complexes **1** and **2** are 13.5% and 13.8%, respectively. The H···N/N···H contacts provide a 1.6% and 20.6% contribution to the total Hirshfeld surface of complexes **1** and **2**, respectively. The other intermolecular contacts such as O···O, C···C, C···N/N···C, C···O/O···C, C···Br/Br···C, and O···Br/Br···O have a negligible effect on the crystal packing. Figure 3 shows the intermolecular interaction percentages from the Hirshfeld Surface analyses of complex **1** (a) and complex **2** (b).

3.4 | Optical properties

UV-vis measurements of complexes **1** and **2** were examined at a concentration of 1×10^{-5} M and in highly polar solvents such as DMSO, DMF, PBS, and water (Figure 4). The absorption maximum of the cobalt complex is 259 nm (logε = 4.89), and the absorption maximum of the nickel complex is 264 nm (logε = 4.96). The nickel complex is 731 cm^{-1} (5 nm) red-shifted (Stokes shift) relative to the cobalt complex. In the spectra taken in DMF and DMSO, the peaks of the bands could not be determined exactly due to the spectral cutoff.

When the aggregation behaviors of complexes **1** and **2** are examined in PBS, it is seen that both compounds do not deviate from the ideal at 10 different concentrations (1–10 μM) and do not exhibit any aggregation. The coefficients of determination for complexes **1** and **2** are 0.9974 and 0.9999, respectively, and the graphs are linear. As the concentration increases or decreases, no new bands are formed in the spectra, and it is compatible with the Lambert–Beer law.

TABLE 2 Selected geometric parameters for the Co(II) (**1**) and Ni(II) (**2**) complexes (Å, °)

1					
Co-O2	2.032(2)	Co-O3	2.141(2)	Co-N1	2.177(3)
Br-C12	1.921(3)	O2-C7	1.311(3)	N1-C6	1.342(3)
O2-Co-O2^{i}	180.0	O2-Co-O3^{i}	93.9(3)	O2-Co-O3	86.1(3)
O2-Co-O3^{i}	93.9(3)	O3-Co-O3^{i}	180.0	O2-Co-N1	90.7(3)
O2-Co-N1	90.7(3)	O2-Co-N1^{i}	89.3(3)	O3-Co-N1	91.8(3)
O2-Co-N1^{i}	89.3 (5)	N1-Co-N1^{i}	180.0	C7-O2-Co	125.6(5)
Symmetry code (i) 1 − x,1 − y,1 − z					
2					
Ni-O1	1.992(2)	Ni-O3	2.068(2)	Ni-N1	2.116(2)
Br-C2	1.851(3)	O1-C7	1.330(3)	N1-C8	1.339(3)
O1-Ni-O1^{i}	180.0	O1-Ni-O3^{i}	94.8(5)	O1-Ni-O3	85.2 (3)
O3-Ni-O3^{i}	180.0	O1-Ni-N1^{i}	86.6(4)	O3-Ni-N1^{i}	91.1(3)
N1-Ni-N1^{i}	180.0	C12-N1-Ni	121.2(5)	C8-N1-Ni	117.3(5)
Symmetry code (i) 1 − x,1 − y,1 − z					

TABLE 3 Hydrogen-bond geometry for complexes **1** and **2** (Å, °)

D-H···A	D-H	H···A	D···A	<D-H···A	Symmetry (i)
1					
O3-H···O5^{i}	0.93	2.43	2.782(2)	102	1 − x,2 − y,1 − z
O3-H···O4^{i}	0.93	2.12	2.980(5)	152	−1/2 + x,3/2 − y,−1/2 + z
O3-H···O1^{i}	0.93	1.89	2.606(5)	132	1 − x,1 − y,1 − z
O4-H···O5	0.82	2.41	2.860(4)	116	1 − x,1 − y,1 − z
C5-H5···O2	0.93	2.54	3.070(5)	117	
C6-H6···O2	0.93	2.53	3.022(2)	113	1 − x,1 − y,1 − z
Br···O1^{i}			3.156(5)		−1/2 + x,1/2 − y,−1/2 + z
2					
O3-H···N2^{i}	0.93	2.36	3.120(5)	138	-1/2 + x,3/2 − y,−1/2 + z
O3-H···O2^{i}	0.93	1.85	2.550(5)	130	1 − x,1 − y,1 − z
C1-H···O1	0.93	2.42	2.740(5)	100	
O10-H···O2^{i}	0.93	2.58	3.410(5)	150	x,1 + y,z
O12-H···O1	0.93	2.48	2.938(4)	110	1 − x,1 − y,1−z
Br···O2^{i}			3.167(5)		−1/2 + x,1/2 − y,−1/2 + z

3.5 | BSA binding studies with spectrofluorometer

BSA is a serum albumin protein and is present in the blood. For drug molecules to circulate in the body through the blood, binding to serum albumin and being easily transported are very important for the treatment process. Studies of complexes **1** and **2** binding to BSA were determined by observing a decrease in BSA emission with increasing ligand concentration at room temperature. BSA has an emission at ∼340 nm due to two tryptophan amino acids (Trp-134 and Trp-213).[51–55] As the ligands interact with these amino acids, the fluorescence of BSA is quenched; that is, the ligands bind to BSA (Figure 5).

Considering the Stern–Volmer binding constant (K_{sv}) of the cobalt and nickel complexes, it is 0.97 L·mol^{-1} ($\times 10^4$) for the cobalt complex and 0.85 L·mol^{-1} ($\times 10^4$) for the nickel complex. The quenching rate constant (K_q) is 0.10 L·mol^{-1} s^{-1} for cobalt and 0.09 L·mol^{-1} s^{-1} for nickel. Within the framework of all these results, the cobalt and nickel complexes have similar binding properties to BSA, but the cobalt complex is slightly better than the nickel complex.

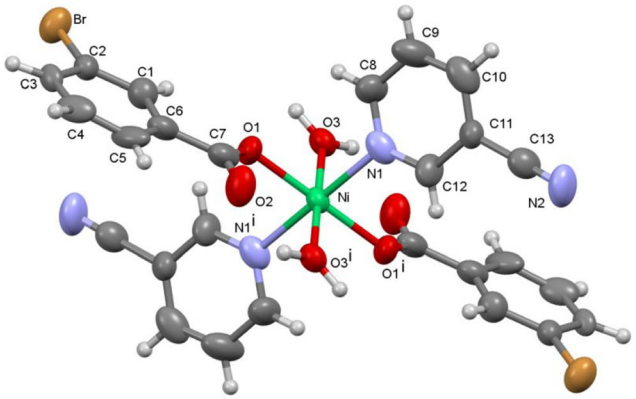

(a)

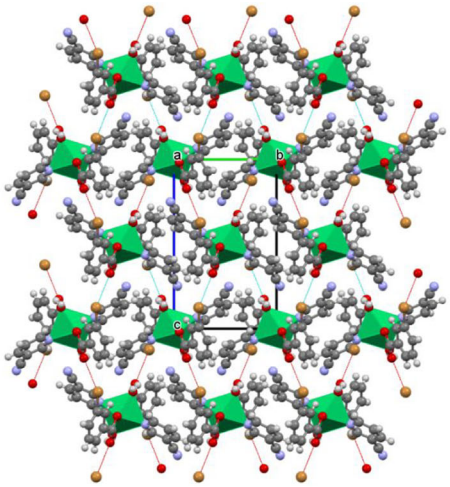

(b)

FIGURE 2 (a) Molecular structure of the Co(II) complex **2** with atom labeling. Displacement ellipsoids were drawn at the 40% probability level. (b) 2D-coordination polyhedra around the Co^{II} atoms with the unit cell viewed down along the *a*-axis. Dashed red lines indicate 2D halogen and H-bonding networks in complex **2**. Symmetry (i) 1 − x,1 − y,1 − z

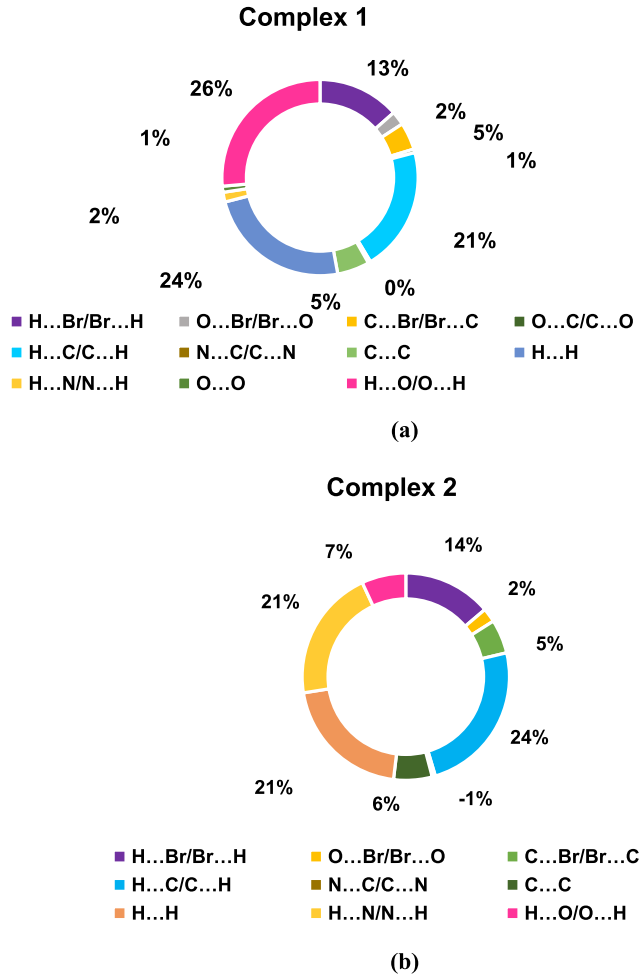

FIGURE 3 The percentages of the intermolecular interactions from obtained Hirshfeld Surface analysis of complex **1** (a) and complex **2** (b)

3.6 | Cytotoxicity

In order for a compound to be recommended as a potential drug, it is important to know its effects on healthy cells.[56] Although theoretical pre-evaluation studies of structure–activity relations have gained popularity today, experimental studies are of great importance. Therefore, in this study, the effects of complexes **1** and **2** on human blood lymphocyte cells were investigated by the MTT method. When the effects of the complexes on the viability of human blood lymphocyte cells were evaluated in the concentration range of 1000–7.81 μg/ml, it was determined that the cell viability did not fall below 50% at any concentration. When the graph in Figure 6 is examined, it is clearly seen that complexes **1** and **2** caused cytotoxic effects due to increasing concentration. It was determined that complex **1** caused 45.31%–33.84% cell death in the concentration range of 1000–7.81 μg/ml, while complex **2** caused 39.03%–31.15% cell death in the same concentration range. When the literature data are evaluated, it is thought that both complexes cause moderate cytotoxicity on human peripheral blood lymphocyte cells.[57]

3.7 | Molecular docking studies

Molecular docking is a useful computational approach for predicting the interaction between a ligand and proteins that have been targeted at the atomic level.[58] In this study, molecular docking analysis of complexes **1** and **2** with the targeted proteins associated with spike proteins of coronavirus variants (SARS-CoV-2 S-Beta variant [B.1.351] [PDB ID:7V76]),[59] (SARS-CoV-2 S-Gamma variant [P.1], [PDB ID: 7V78]),[60] (SARS-CoV-2

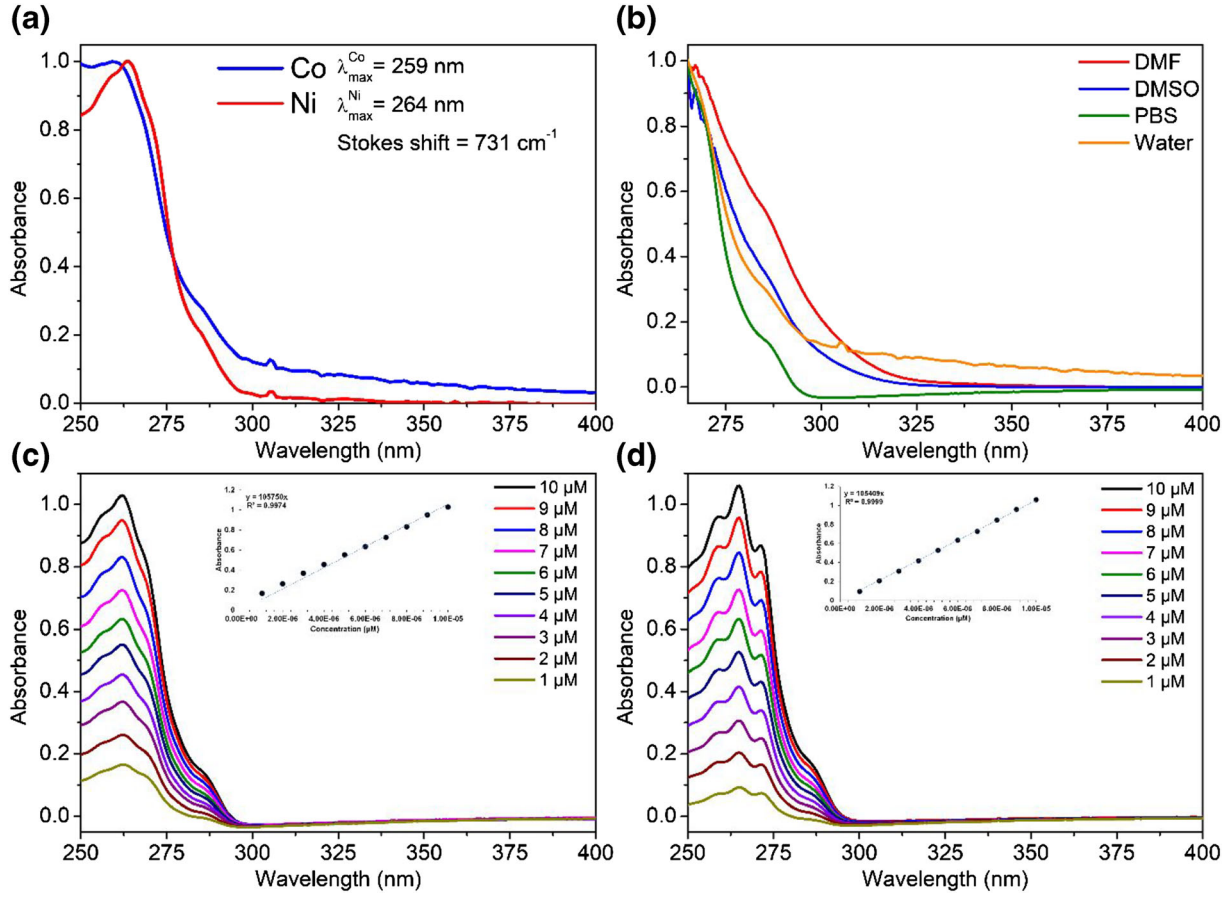

FIGURE 4 (a) UV-vis absorption spectra of complexes **1** and **2** in water. (b) Complex **1** absorption spectra in different solvents. (c) Complex **1** absorption spectra with a different concentration in PBS. (d) Complex **2** absorption spectra with a different concentration in PBS

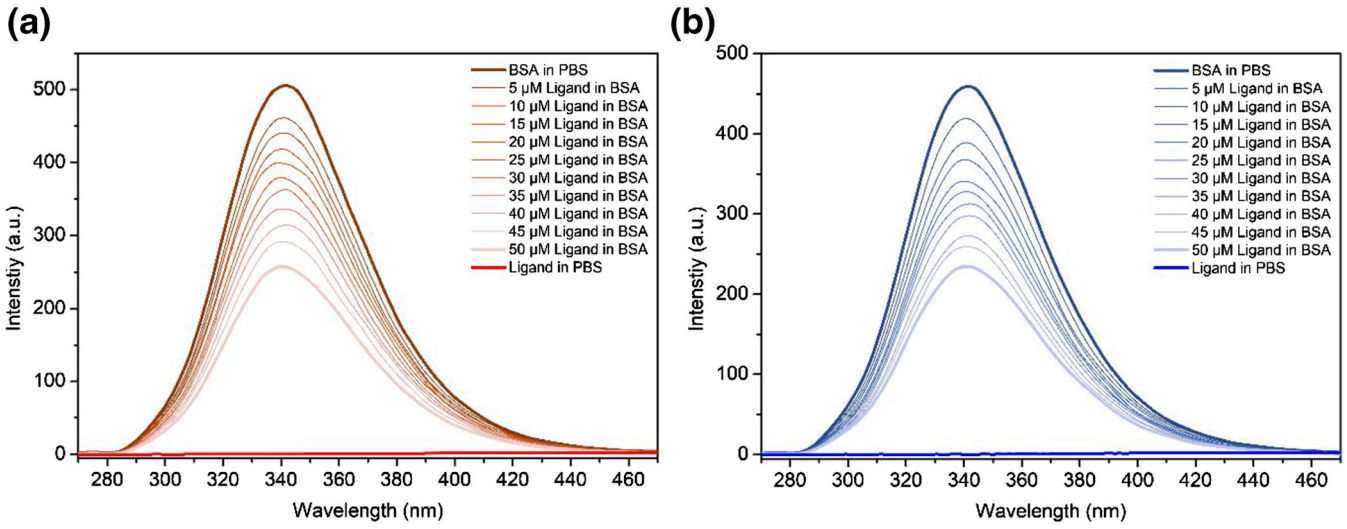

FIGURE 5 Fluorescence spectra of (a) complex —BSA with increasing concentration of complex **1**. Fluorescence spectra of (b) complex **2**—BSA with increasing concentration of complex **2**

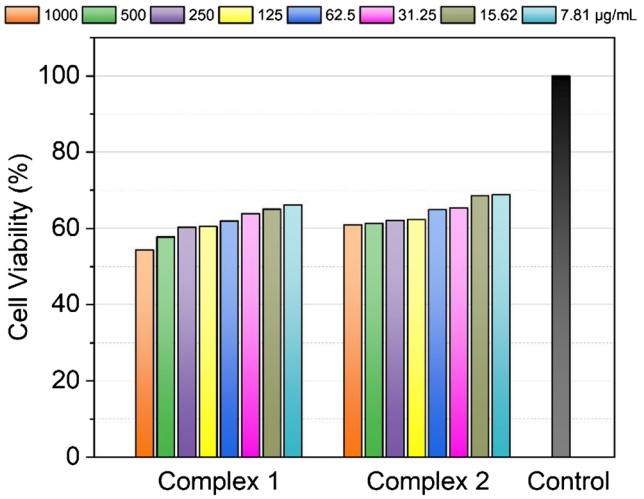

FIGURE 6 Effect of complexes **1** and **2** on blood lymphocyte cells' cell viability

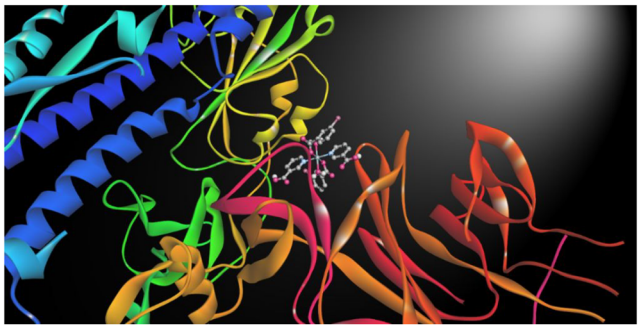

FIGURE 7 Three-dimensional representation of complex **1** and spike protein of the kappa variant of SARS CoV-2

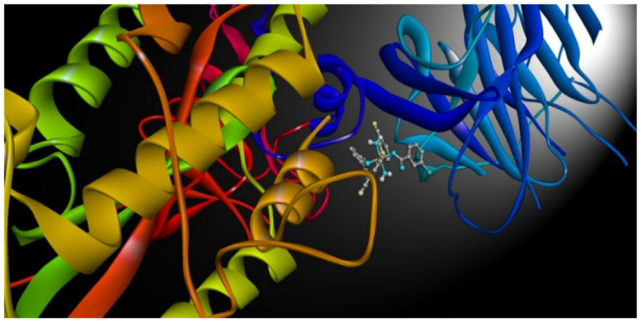

FIGURE 8 Three-dimensional representation of complex **2** and spike protein of the beta variant of SARS CoV-2

S-Delta variant [B.1.617.2] [PDB ID: 7V7N]),[61] (SARS-CoV-2 S-Kappa variant [B.1.617.1] [PDB ID: 7V7D]),[62] and (SARS-CoV-2 Omicron variant [B.1.1.529] spike protein [WNT7A {PDB ID: 7T9J}])[63] were carried out. Spike protein is one of the most significant targets in the search for coronavirus drugs. This is due to the spike protein's ability to connect to the angiotensin-converting enzyme 2 (ACE2) receptors in human cells, making the virus more infectious.[64] Table S2 displays the docking scores and detailed interactions between complexes **1**, **2**, and targets. The lower the docking score, the better the ligand–protein interaction. According to the molecular docking studies, the binding energies between complex **1** and 7V76, 7V78, 7V7N, 7V7D, and 7T0J targets were -7.06 ± 0.33, -6.75 ± 0.11, -7.03 ± 0.24, -7.16 ± 0.14, and 6.65 ± 0.05 kcal/mol, respectively. The binding energies between complex **2** and **1** 7V76, 7V78, 7V7N, 7V7D, and 7T0J targets were -7.63 ± 0.029, -6.90 ± 0.41, -7.20 ± 0.07, -6.97 ± 0.15, and 6.98 ± 0.06 kcal/mol, respectively. While the binding affinity of complex **1** to the spike proteins of gamma and omicron variants of SARS CoV-2 is more predominant, the binding affinity of complex **2** to spike proteins of its beta, gamma, and delta variants is more predominant. These results showed that complex **1** exhibits the strongest binding affinity against the active site of the spike protein of the kappa variant (Figures 7 and S5), while complex **2** exhibits the strongest binding affinity against the active site of the spike protein of the beta variant (Figures 8 and S6). It is thought that functional groups such as aromatic rings (phenyl and pyridine), carboxylate, cyano-, bromo-, and hydroxyl-groups (from coordinated water molecules) in the crystal structure of complexes **1** and **2** have an important effect on the diversity of interactions with the active site of spike proteins. There are hydrophobic and electrostatic interactions such as π-anion, π-cation, π-alkyl, π-π stacking, alkyl, amide-π stacking, π-π T-shaped, carbon-hydrogen bond, and π-sigma as well as hydrogen bonding between the complexes and the active sites of the spike proteins of the coronavirus beta, gamma, delta, kappa, and omicron variants. The formation of hydrogen bonds is an important factor influencing the integrity and stability of any protein-ligand interaction.[18] Conventional hydrogen bonds are the only common interactions found between complexes **1** and **2** and the active sites of the spike proteins of the investigated variants. The average hydrogen bond distances between complex **1** and with Leu514, Asp425, and Glu513 amino acids of 7V76; Ans81, Arg237, Gln239, Asn137, and Thr22 amino acids of 7V78; Gly28 and Arg44 amino acids of 7V7N; Thr51, Lys202, Pro39, Asp53, and Asp228 amino acids of 7V7D; and His1058, Asp867, and Val952 amino acids of 7T9J were found as 2.14, 2.34, 2.58, 2.68, and 2.60 Å, respectively. The average hydrogen bond distances between complex **2** and with Asp287, Ser294, Lys297, and Asn603 amino acids of 7V76; Gln239 and Asn137 amino acids of 7V78; Arg271, Arg632, Ala290 and Leu291 amino acids of

7V7N; Lys195 and Pro39 amino acids of 7V7D; and His1058 amino acid of 7T9J were found as 2.68, 2.47, 2.64, 2.36, and 2.31 Å, respectively. These bond distances show that these two complexes make strong hydrogen bond interactions with the active site of the spike protein of SARS CoV-2 variants.[65] Consequently, the low binding energies and interaction diversity can be attributed to the bioactive nature of complexes **1** and **2**.

The binding of drug candidate molecules to the blood serum and the circulation of these drugs in the body is important. The binding of complexes **1** and **2** to serum albumin was investigated experimentally and supported by theoretical calculations. BSA (PDB: 4OR0)[66] was used in serum albumin molecular docking studies. As a result of docking the ligands to the active site of BSA, the scores are -9.65 ± 0.04 for complex **1** and -9.32 ± 0.09 kcal/mol for complex **2**. Binding scores in this study are highly effective compared with other docking studies and comply with experimental results $\Delta G^{Co(II)} > \Delta G^{Ni(II)}$. In this context, it can be said that the complexes can be easily transported through the blood in the body and do not undergo any precipitation since they are dissolved in water; 3D representation of complexes **1** (a) and **2** (b) with BSA was given in Figure 9.

3.8 | DFT

The molecular structures of complexes **1** and **2** were optimized by the DFT method. The 3D structures of the complexes were obtained from the crystal information file (cif). The electronic energies, polarizability, dipole moments, ionization potentials, electron affinities, electronegativity, chemical hardness, global softness, electrophilic indexes, HOMO-LUMO orbitals, and band gaps of the complexes were calculated from obtained DFT data. The Koopmans theorem[67] states that the ionization potential and electron affinity are related to the orbital energies of HOMO and LUMO. The electron affinity is equal to the positive value of the HOMO energy and the ionization potential is equal to the positive value of the LUMO energy (EA = |−HOMO|; IP = |−LUMO|). The electronegativity (χ) values were calculated using $\chi = (IP + EA)/2$.[68] The chemical hardness (η) and softness (σ) were obtained by using $\eta = (IP\text{-}EA)/2$ and $\sigma = 1/\eta$,[69–71] respectively. Electrophilic indexes (ω) were calculated by the formula $\omega = \chi^2/2\eta$.[72]

The optimized geometries of the molecules did not deviate from the experimental bond length, bond angles, and torsion angle values. The electronic energies of the molecular systems are −228507.89 eV for the cobalt complex and −226679.52 eV for the nickel complex. Cobalt complex **1** has lower energy than nickel complex **2**. Cobalt complex **1** has higher polarizability and is more polar than nickel complex **2**. The nickel complex has a high electron affinity and thus a greater electronegativity. The HOMO-LUMO of complex **1** is −6.42 and −2.51 eV, respectively, and the band gap is 3.91 eV. The HOMO-LUMO of complex **2** is −6.61 and −2.60 eV, respectively, and the band gap is 4.01 eV. The cobalt complex has a narrower band gap than the nickel complex and is a molecule with higher activity (Figure 10).

The HOMO−1 and HOMO orbitals of the cobalt complex are on the central cobalt metal and coordinated crystalline water and migrated onto nicotinic acid by metal-to-ligand charge transfer (MLCT). The LUMO and LUMO+1 orbitals are located on nicotinic acid. The 3-bromobenzoic acid group did not contribute to the cobalt complex orbitals. In the nickel complex, the HOMO-1 orbitals are on the 3-bromobenzoic acid group, while the HOMO orbitals are on the central nickel metal and coordinated crystalline water. LUMO and LUMO+1

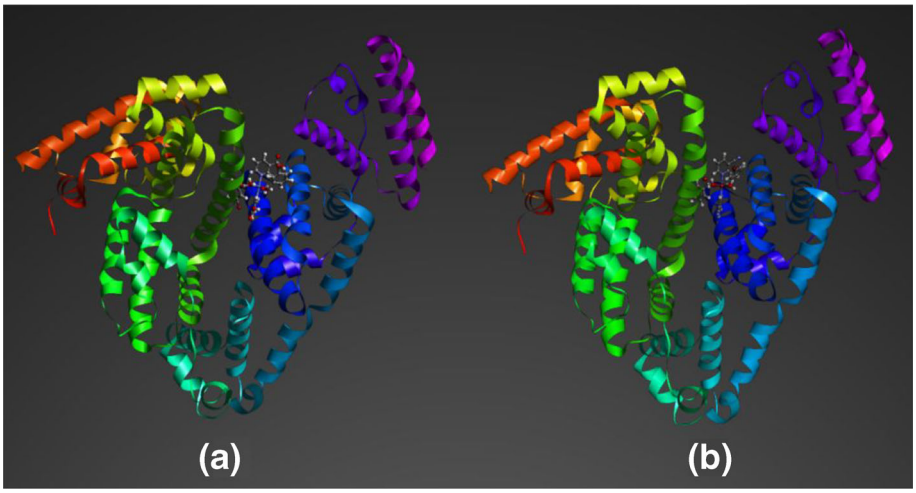

FIGURE 9 Three-dimensional representation of complexes **1** (a) and **2** (b) with BSA

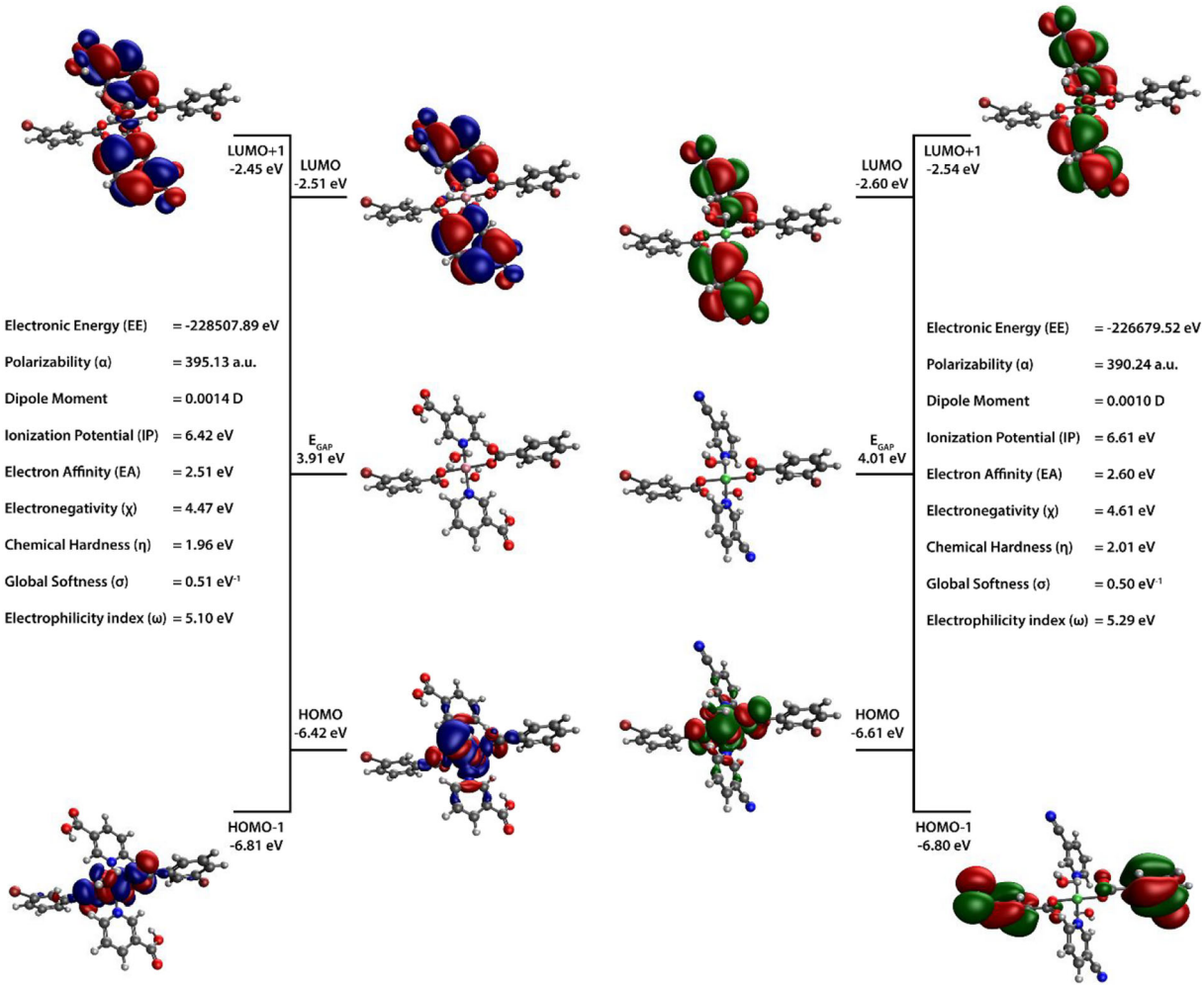

FIGURE 10 HOMO-LUMO orbitals and calculated DFT parameters of complexes **1** and **2**

orbitals migrated onto the nicotinonitrile group by metal-to-ligand charge transfer (MLCT). All these computational results show that the properties of nickel and cobalt complexes are similar.

3.9 | Estimated pharmacokinetic and toxicokinetic properties

Predicting the pharmacokinetic and toxicokinetic properties of therapeutic candidate molecules increases the likelihood of successful drug development. Lipinski and colleagues proposed five principles for identifying whether a compound is a drug.[73] According to the results obtained, Lipinski's five criteria are compatible with complex **2** with one exception. Due to their bulkiness, complexes **1** and **2** can be used as a P-glycoprotein substrate even if they cannot cross the blood–brain barrier (BBB). They have a poor rate of gastrointestinal absorption. The solubility in octanol/water of complexes **1** and **2** is low due to their rigid structure. Complex **1** does not interact with cytochrome P450 enzymes (CYPs) such as CYP2D6 and CYP2C9, and it interacts with CYP1A2, CYP2C19, and CYP3A4 inhibitors. Complex **2** does not interact with CYP1A2 and CYP2D6 and it interacts with CYP2C19, CYP2C9, and CYP3A4 inhibitors. When the estimated toxicity levels were evaluated, the complexes were determined to be nontoxic. The similarity with the compounds used in the estimation of toxicity is ~27.00%. The estimated lethal dose amount for complexes **1** and **2** are 930 and 700 mg/kg, respectively. Complexes **1** and **2** are non-toxic in terms of hepatotoxicity, carcinogenicity, immunotoxicity, mutagenicity, cytotoxicity, and mitochondrial membrane potential (MMP). Given all of these advantages and disadvantages, complexes **1** and **2** are regarded to be pharmacological candidates. Table 4 shows the estimated pharmacokinetic characteristics of complexes **1** and **2**.

TABLE 4 The pharmacokinetic properties of complexes **1** and **2**

Properties	1	2
Molecular weight (g/mol)	741.2	702.96
Heavy atoms	41	39
Rotatable bonds	10	8
H-Bond acceptors	8	8
H-Bond donors	4	2
Molar refractivity	149.87	143.11
TPSA ($Å^2$)	167.10	128.50
Log $P_{o/w}$	3.84	5.52
GI absorption	Low	Low
BBB permeant	No	No
P-gp substrate	No	No
CYP1A2 inhibitor	Yes	No
CYP2C19 inhibitor	Yes	Yes
CYP2C9 inhibitor	No	Yes
CYP2D6 inhibitor	No	No
CYP3A4 inhibitor	Yes	Yes
Log K_p (cm/s)	−8.08	−6.67
Lipinski	No	Yes
Toxicity class[a]	4	4
Predicted LD_{50}	930 mg/kg	700 mg/kg
Hepatotoxicity	Inactive	Inactive
Carcinogenicity	Inactive	Inactive
Immunotoxicity	Inactive	Inactive
Mutagenicity	Inactive	Inactive
Cytotoxicity	Inactive	Inactive
MMP[b]	Inactive	Inactive

[a]The toxicity class consists of six numbers. (Number 1 means toxic; number 6 means non-toxic.)
[b]MMP: mitochondrial membrane potential.

4 | CONCLUSION

In this study, the pyridine 3-carboxylate complex of Co(II) 3-bromobenzoate and 3-cyanopyridine complex of Ni(II) 3-bromobenzoate were successfully synthesized, and their structure was characterized utilizing single crystal X-ray diffraction, FT-IR, and elemental analysis. For both complexes, the bivalent Co^{2+} and Ni^{2+} ions are coordinated by four oxygen atoms and two nitrogen atoms to form MO_4N_2 octahedral coordination geometry. Complexes **1** and **2** crystallize in the monoclinic space group $P2_1/n$. It has been determined that H···H and H···O/O···H interactions contribute greatly to the Hirshfeld surface and the stability of the crystal structure. Fluorescent quenching technique and Molecular Docking studies showed that both complexes exhibit a strong binding affinity to BSA. The fluorescence spectra indicate that increasing concentrations of both complexes influence the active sites of BSA, showing that conformational changes occur in these regions of BSA in the presence of the complexes. This is supported by the binding affinity and types found by molecular docking studies. With the help of in vitro cytotoxicity studies, both complexes were determined to cause moderate cytotoxicity on human peripheral blood lymphocyte cells. When the interactions of both complexes with the spike protein of beta, gamma, delta, kappa, and omicron variants of SARS CoV-2 were examined with the help of molecular docking and evaluated in terms of binding energies, it is found that complexes **1** and **2** were effective in inhibiting the spike protein of the kappa variant of SARS CoV-2 and spike protein of the beta variant of SARS CoV-2, respectively. Considering the BSA binding affinity, pharmacokinetic and toxicological properties, and cytotoxicity on human blood lymphocyte cells, further in vivo and in vitro studies are recommended to determine the potential drug properties of complex **1**.

ACKNOWLEDGMENTS

The authors thank the Kafkas University Research Fund for financial support under Grant Number 2018-FM-66. The numerical calculations reported in this paper were fully performed at TUBITAK ULAKBIM, High Performance and Grid Computing Center (TRUBA resources). We are grateful to the Turkish Chemical Society for their support.

AUTHOR CONTRIBUTIONS

Füreya Elif Öztürkkan: Conceptualization; Data curation; Investigation; Methodology; Project administration; Resources; Software; Supervision; Validation; Visualization; Writing – original draft. **Mücahit Özdemir**: Conceptualization; Investigation; Methodology; Software; Supervision; Validation; Visualization; Writing – original draft. **Giray Buğra Akbaba**: Investigation; Methodology; Writing – original draft. **Mustafa Sertçelik**: Investigation; Methodology; Project administration. **Bahattin Yalçın**: Conceptualization; Investigation; Methodology. **Ertan Şahin**: Data curation; Methodology; Project administration; Software; Visualization; Writing – original draft.

ORCID

Füreya Elif Öztürkkan https://orcid.org/0000-0001-6376-4161
Mücahit Özdemir https://orcid.org/0000-0002-0840-4953
Giray Buğra Akbaba https://orcid.org/0000-0002-1413-

9498
Mustafa Sertçelik https://orcid.org/0000-0001-7919-7907
Bahattin Yalçın https://orcid.org/0000-0003-4448-1101
Ertan Şahin https://orcid.org/0000-0002-6311-8917

REFERENCES

[1] Y. M. Issa, S. A. Abdel-Latif, A. L. El-Ansary, H. B. Hassib, *New J. Chem.* **2021**, *45*, 1482.
[2] S. A. Abdel-Latif, A. A. Mohamed, *J. Mol. Struct.* **2018**, *1156*, 712.
[3] S. A. Abdel-Latif, H. Moustafa, *Appl. Organomet. Chem.* **2018**, *32*, e4269.
[4] N. Uddin, M. Sirajuddin, S. Ali, Potentially Bioactive Carboxylate Complexes of Transition Metals Transition Metal Carboxylate Complexes, **2015**.
[5] A. Nandy, C. Duan, M. G. Taylor, F. Liu, A. H. Steeves, H. J. Kulik, *Chem. Rev.* **2021**, *121*, 9927.
[6] N. S. Abdel-Kader, S. A. Abdel-Latif, A. L. El-Ansary, A. G. Sayed, *J. Mol. Struct.* **2021**, *1223*, 129203.
[7] N. S. Abdel-Kader, S. A. Abdel-Latif, A. L. El-Ansary, A. G. Sayed, *New J. Chem.* **2019**, *43*, 17466.
[8] V. Zelenák, K. Györyová, D. Mlynarcík, *Met.-Based Drugs* **2002**, *8*, 269.
[9] M. Bingöl, N. Turan, *J. Mol. Struct.* **2020**, *1205*, 127542.
[10] R. Zafar, M. Zubair, S. Ali, K. Shahid, W. Waseem, H. Naureen, A. Haider, M. S. Jan, F. Ullah, M. Sirajuddin, A. Sadiq, *J. Biomol. Struct. Dyn.* **2021**, *39*, 1044.
[11] M. Iqbal, S. Ali, M. N. Tahir, *J. Coord. Chem.* **2018**, *71*, 991.
[12] Y. Menuchin-Lasowski, A. Schreiber, A. Lecanda, A. Mecate-Zambrano, L. Brunotte, O. E. Psathaki, S. Ludwig, T. Rauen, H. R. Schöler, *Stem Cell Rep.* **2022**, *17*, 789.
[13] S. A. Meo, A. M. Alhowikan, T. Al-khlaiwi, I. M. Meo, D. M. Halepoto, M. Iqbal, A. M. Usmani, W. Hajjar, N. Ahmed, *Eur. Rev. Med. Pharmacol. Sci.* **2020**, *24*, 2012.
[14] P. A. Christensen, R. J. Olsen, S. W. Long, R. Snehal, J. J. Davis, M. Ojeda Saavedra, K. Reppond, M. N. Shyer, J. Cambric, R. Gadd, R. M. Thakur, A. Batajoo, R. Mangham, S. Pena, T. Trinh, J. C. Kinskey, G. Williams, R. Olson, J. Gollihar, J. M. Musser, *Am. J. Pathol.* **2022**, *192*, 642.
[15] H. Gu, P. Krishnan, D. Y. M. Ng, L. D. J. Chang, G. Y. Z. Liu, S. S. M. Cheng, M. M. Y. Hui, M. C. Y. Fan, J. H. L. Wan, L. H. K. Lau, B. J. Cowling, M. Peiris, L. L. M. Poon, *Emerg. Infect. Dis.* **2022**, *28*, 460.
[16] N. Ali, R. Khan, A. F. AlAsmari, V. Kumar, *Process Biochem.* **2022**, *115*, 70.
[17] A. Pandey, A. N. Nikam, A. B. Shreya, S. P. Mutalik, D. Gopalan, S. Kulkarni, B. S. Padya, G. Fernandes, S. Mutalik, R. Prassl, *Life Sci.* **2020**, *256*, 117883.
[18] S. Houchi, Z. Messasma, *J. Mol. Struct.* **2022**, *1263*, 133032.
[19] M. Frisch, G. Trucks, H. Schlegel, G. Scuseria, M. Robb, J. Cheeseman, G. Scalmani, V. Barone, B. Mennucci, G. Petersson, H. Nakatsuji, M. Caricato, X. Li, H. Hratchian, A. Izmaylov, J. Bloino, G. Zheng, J. Sonnenberg, M. Hada, M. Ehara, K. Toyota, R. Fukuda, J. Hasegawa, M. Ishida, T. Nakajima, Y. Honda, O. Kitao, H. Nakai, T. Vreven, J. Montgomery, J. Peralta, F. Ogliaro, M. Bearpark, J. Heyd, E. Brothers, K. Kudin, V. Staroverov, R. Kobayashi, J. Normand, K. Raghavachari, A. Rendell, J. Burant, S. Iyengar, J. Tomasi, M. Cossi, N. Rega, J. Millam, M. Klene, J. Knox, J. Cross, V. Bakken, C. Adamo, J. Jaramillo, R. Gomperts, R. Stratmann, O. Yazyev, A. Austin, R. Cammi, C. Pomelli, J. Ochterski, R. Martin, K. Morokuma, V. Zakrzewski, G. Voth, P. Salvador, J. Dannenberg, S. Dapprich, A. Daniels, O. Farkas, J. Foresman, J. Ortiz, J. Cioslowski, D. Fox, *Gaussian 09, Revision B.01, Gaussian 09, Revision B.01*, Gaussian, Inc., Wallingford CT **2009**.
[20] G. M. Sheldrick, *Acta Crystallogr. C* **2015**, *71*, 3.
[21] G. M. Sheldrick, *Acta Crystallogr. A: Found. Adv. Crystallogr.* **2008**, *64*, 112.
[22] T. Mosmann, *J. Immunol. Methods* **1983**, *65*, 55.
[23] J. R. Lakowicz, G. Weber, *Biochemistry* **1973**, *12*, 4161.
[24] C.-Q. Jiang, M.-X. Gao, J.-X. He, *Anal. Chim. Acta* **2002**, *452*, 185.
[25] M. Guo, J.-W. Zou, P.-G. Yi, Z.-C. Shang, G.-X. Hu, Q.-S. Yu, *Anal. Sci.* **2004**, *20*, 465.
[26] W. Kohn, L. J. Sham, *Phys. Rev.* **1965**, *140*, A1133.
[27] M. Frisch, G. Trucks, H. Schlegel, G. Scuseria, M. Robb, J. Cheeseman, G. Scalmani, V. Barone, B. Mennucci, G. Petersson, H. Nakatsuji, M. Caricato, X. Li, H. Hratchian, A. Izmaylov, J. Bloino, G. Zheng, J. Sonnenberg, M. Hada, M. Ehara, K. Toyota, R. Fukuda, J. Hasegawa, M. Ishida, T. Nakajima, Y. Honda, O. Kitao, H. Nakai, T. Vreven, J. Montgomery, J. Peralta, F. Ogliaro, M. Bearpark, J. Heyd, E. Brothers, K. Kudin, V. Staroverov, R. Kobayashi, J. Normand, K. Raghavachari, A. Rendell, J. Burant, S. Iyengar, J. Tomasi, M. Cossi, N. Rega, J. Millam, M. Klene, J. Knox, J. Cross, V. Bakken, C. Adamo, J. Jaramillo, R. Gomperts, R. Stratmann, O. Yazyev, A. Austin, R. Cammi, C. Pomelli, J. Ochterski, R. Martin, K. Morokuma, V. Zakrzewski, G. Voth, P. Salvador, J. Dannenberg, S. Dapprich, A. Daniels, O. Farkas, J. Foresman, J. Ortiz, J. Cioslowski, D. Fox, *Gaussian 09, Revision B.01*, Gaussian, Inc., Wallingford CT **2009**.
[28] IQmol Molecular Viewer, can be found under http://iqmol.org/, n.d.
[29] A. D. Becke, *Phys. Rev. a* **1988**, *38*, 3098.
[30] A. D. Becke, *J. Chem. Phys.* **1993**, *98*, 5648.
[31] C. Lee, W. Yang, R. G. Parr, *Phys. Rev. B* **1988**, *37*, 785.
[32] M. A. Spackman, D. Jayatilaka, *CrstEngComm* **2009**, *11*, 19.
[33] P. R. Spackman, M. J. Turner, J. J. McKinnon, S. K. Wolff, D. J. Grimwood, D. Jayatilaka, M. A. Spackman, *J. Appl. Cryst.* **2021**, *54*, 1006.
[34] O. Trott, A. J. Olson, *J. Comput. Chem.* **2009**.
[35] G. M. Morris, D. S. Goodsell, R. S. Halliday, R. Huey, W. E. Hart, R. K. Belew, A. J. Olson, *J. Comput. Chem.* **1998**, *19*, 1639.
[36] BIOVIA, Dassault Systèmes, BIOVA Discovery Studio Visualizer 2021, v21.1.0.20298, San Diego: Dassault Systèmes, **2021**.
[37] A. Daina, O. Michielin, V. Zoete, *Sci. Rep.* **2017**, *7*, 42717.
[38] P. Banerjee, A. O. Eckert, A. K. Schrey, R. Preissner, *Nucleic Acids Res.* **2018**, *46*, W257.
[39] G. Ş. Aşkın, H. Necefoğlu, S. Özkaya, R. Çatak Çelik, T. Hökelek, *Acta Cryst. E* **2016**, *72*, 888.
[40] G. Ş. Aşkın, H. Necefoğlu, G. Yılmaz Nayir, R. Çatak Çelik, T. Hökelek, *Acta Cryst. E* **2015**, *71*, 561.
[41] T. Hökelek, H. Necefouglu, *Acta Crystallogr. C* **1998**, *54*, 1242.

[42] H. Necefoğlu, A. Maracı, F. E. Özbek, B. Tercan, T. Hökelek, *Acta Cryst. E* **2011**, *67*, m619.
[43] T. Hökelek, H. Dal, B. Tercan, F. E. Özbek, H. Necefoğlu, *Acta Crystallogr. E Struct. Rep. Online* **2009**, *65*, m466.
[44] L. J. Bellamy, *The Infrared Spectra of Complex Molecules*, Vol. 1, Chapman And Hall, London **1986**.
[45] P. J. Larkin, *Infrared and Raman Spectroscopy: Principles and Spectral Interpretation*, Elsevier, Amsterdam **2011**.
[46] M. Huseynova, V. Farzaliyev, A. Medjidov, M. Aliyeva, M. Özdemir, P. Taslimi, Y. Zorlu, B. Yalçın, O. Şahin, *J. Mol. Struct.* **2022**, *1248*, 131470.
[47] K. Nakamoto, *Infrared and Raman Spectra of Inorganic and Coordination Compounds*, Wiley, New York **1986**.
[48] D. Jayatilaka, D. J. Grimwood, A. Lee, A. Lemay, A. J. Russel, C. Taylor, S. K. Wolff, P. Cassam-Chenai, A. Whitton, TONTO, http://hirshfeldsurface.net/, **2005**.
[49] J. J. McKinnon, D. Jayatilaka, M. A. Spackman, *Chem. Commun.* **2007**, 3814.
[50] M. A. Spackman, J. J. McKinnon, D. Jayatilaka, *CrstEngComm* **2008**, *10*, 377.
[51] D. M. Togashi, A. G. Ryder, *J. Fluoresc.* **2005**, *16*, 153.
[52] M. Möller, A. Denicola, *Biochem. Mol. Biol. Educ.* **2002**, *30*, 175.
[53] A. Papadopoulou, R. J. Green, R. A. Frazier, *J. Agric. Food Chem.* **2005**, *53*, 158.
[54] N. Tayeh, T. Rungassamy, J. R. Albani, *J. Pharm. Biomed. Anal.* **2009**, *50*, 107.
[55] A. Sułkowska, J. Równicka, B. Bojko, J. Pożycka, I. Zubik-Skupień, W. Sułkowski, *J. Mol. Struct.* **2004**, *704*, 291.
[56] A. Ton, F. Gentile, M. Hsing, F. Ban, A. Cherkasov, *Mol. Inf.* **2020**, *39*, 2000028.
[57] J. van Meerloo, G. J. L. Kaspers, J. Cloos, *Methods Mol. Biol.* **2011**, *731*, 237.
[58] X.-Y. Meng, H.-X. Zhang, M. Mezei, M. Cui, *Curr. Comput. Aided Drug des.* **2011**, *7*, 146.
[59] R. P. D. Bank, RCSB PDB - 7V76: Cryo-EM structure of SARS-CoV-2 S-Beta variant (B.1.351), uncleavable form, one RBD-up conformation, can be found under https://www.rcsb.org/structure/7V76, n.d.
[60] R. P. D. Bank, RCSB PDB - 7V78: Cryo-EM structure of SARS-CoV-2 S-Gamma variant (P.1), one RBD-up conformation 1, can be found under https://www.rcsb.org/structure/7V78, n.d.
[61] R. P. D. Bank, RCSB PDB - 7V7N: Cryo-EM structure of SARS-CoV-2 S-Delta variant (B.1.617.2), all RBD-down conformation, can be found under https://www.rcsb.org/structure/7V7N, n.d.
[62] R. P. D. Bank, RCSB PDB - 7V7D: Cryo-EM structure of SARS-CoV-2 S-Kappa variant (B.1.617.1), all RBD-down conformation, can be found under https://www.rcsb.org/structure/7V7D, n.d.
[63] R. P. D. Bank, RCSB PDB - 7T9J: Cryo-EM structure of the SARS-CoV-2 Omicron spike protein, can be found under https://www.rcsb.org/structure/7T9J, n.d.
[64] Y. Wan, J. Shang, R. Graham, R. S. Baric, F. Li, *J. Virol.* **2020**, *94*, e00127-20. https://doi.org/10.1128/JVI.00127-20
[65] W. W. Cleland, *Arch. Biochem. Biophys.* **2000**, *382*, 1.
[66] A. Bujacz, K. Zielinski, B. Sekula, *Proteins* **2014**, *82*, 2199.
[67] T. Koopmans, *Physica* **1934**, *1*, 104.
[68] R. S. Mulliken, *J. Chem. Phys.* **1934**, *2*, 782.
[69] R. G. Pearson, *J. Chem. Educ.* **1987**, *64*, 561.
[70] R. G. Parr, P. K. Chattaraj, *J. Am. Chem. Soc.* **1991**, *113*, 1854.
[71] R. G. Parr, R. G. Pearson, *J. Am. Chem. Soc.* **1983**, *105*, 7512.
[72] R. G. Parr, L. V. Szentpály, S. Liu, *J. Am. Chem. Soc.* **1999**, *121*, 1922.
[73] C. A. Lipinski, F. Lombardo, B. W. Dominy, P. J. Feeney, *Adv. Drug Deliv. Rev.* **1997**, *23*, 3.

SUPPORTING INFORMATION

Additional supporting information can be found online in the Supporting Information section at the end of this article.

How to cite this article: F. E. Öztürkkan, M. Özdemir, G. B. Akbaba, M. Sertçelik, B. Yalçın, E. Şahin, *Appl Organomet Chem* **2023**, *37*(3), e7021. https://doi.org/10.1002/aoc.7021